Abstract

Design, Modeling, and Control
Strategies for Soft Robotics

In the past two decades, the field of soft robotics has sparked significant interest among many scientific disciplines. Contrary to rigid robots, soft robots explore soft materials that significantly enhance the robot's dexterity, enable a rich family of motion primitives, and enhance environmental robustness regarding contact and impact. Since its inception, soft robotics has exemplified its potential in diverse areas such as safe manipulation, adaptive grasping, exploration under environmental uncertainty, rehabilitation, and the bio-mimicry of many animals. By exploring the uncharted versatile nature of soft materials, soft robotics places the first steppingstones towards achieving biological performance in modern-day's robotics. This thesis aims to further the advances in soft robotics by addressing some of the open multi-disciplinary challenges within this young field of research.

Although soft materials harbor many advantages akin to biology, which are difficult to achieve for rigid robotics, it also roots many fundamental problems. First is the issue of soft robotic design. Traditional robotic design emphasizes high structural rigidity and weight minimization – a well-established practice in engineering. On the other hand, soft robotic design relishes minimal structural rigidity for motion, leading to complex, highly nonlinear relations between the input and output. Besides, distributed soft actuation, imparted by gravitational and inertial effects acting on the elastic continuum body, introduce joint mobilities that are in many cases uncontrollable nor aligned with the control objective, *e.g.*, grasping and manipulation. As describing the underlying continuum mechanics and applying such mathematical theory to the systematic design of soft robots is challenging, a large number of soft robotic systems are still developed *ad hoc*.

Second, a direct duality of the previous challenge, is dealing with the innate infinite-dimensionality from a modelling perspective – particularly with model-based feedback in mind. The transition from rigid to flexible has introduced a new control paradigm: the trade-off between precision and speed in a numerical setting. Not only is control theory for soft robotics in stages of inception, but deriving accurate and numerically efficient model-based controllers is challenging due to large nonlinear deformations of the soft robotic continuum.

In light of these challenges, this thesis proposes a set of systematic tools with theoretical and experimental applications for (*i*) the structural design and fabrication of continuum-deformable soft actuators optimized for user-defined joint motion, (*ii*) the development of efficient dynamic models of soft continuum manipulators, and (*iii*) applying such mathematical models to model-based controllers

for a subclass of (pneumatic) soft continuum manipulators and soft grippers.

The first part of the thesis addresses the design problem by proposing novel computer-automated design algorithms for developing efficient soft actuators. These algorithms account for the underlying continuum mechanics described by a set of partial differential equations, which respects the aforementioned nonlinearities between the input and output motion. Tailoring a user-defined objective to a desired motion and control reachability, an implicit representation of the optimal soft material distribution can be found within a fixed design space. Several generative designs for a diverse subset of soft actuation morphologies are produced including, but not limited to, soft rotational actuators, soft artificial muscles, and soft grippers. In what follows, an optimal design for a soft robotic manipulator with an adaptive gripper is synthesized; and through Additive Manufacturing (AM) of printable flexible material, the sim-to-real boundary is passed. The proposed approach does not only accelerate design convergence, it also builds upon the vast library of soft robot morphologies currently unexplored in literature.

The second part of the thesis addresses the question on modeling for control applicable to a class of soft robotic systems – most notably soft continuum manipulators. The thesis proposes a reduced-order modeling strategy for soft robotics, whose dynamics are derived through differential geometric theory on spatial beams. Besides discussing earlier modeling strategies, the thesis also proposes a new strain-based parametrization approach that ensures the structural geometry information and the underlying continuum mechanics are preserved when synthesizing the reduced-order beam models – a possible solution to the aforementioned control paradigm of precision vs. speed. To enhance numerical performance further, spatio-temporal integration schemes are also proposed that exploit the geometric structure of such soft beam models, resulting in real-time simulation with sufficient numerical precision purposefully tailored for control.

The third part of the thesis treats the development of model-based controllers that can be employed in various control scenarios akin to control for traditional rigid robotics, *e.g.*, inverse kinematics and motion planning, set-point stabilization, trajectory tracking, and multi-point grasping of objects. The stabilizing controller is rooted in an energy-based formulism, providing robustness even when faced with material uncertainties. The controller's effectiveness is demonstrated both in simulation and experiments for various soft robotic systems that share a resemblance to biology, *e.g.*, the elephant's trunk or the tentacle of an octopus.

The main contribution of the thesis is a collection of multi-disciplinary tools compressed into one general framework for the design, modeling, and control of a class of soft robots, ranging from the theoretical to the experimental domain.

Keywords: Soft Robots, Hyper-redundant Robots, Design Optimization, Continuum Mechanics, Reduced-order Modeling, Model-based Control, Additive Manufacturing.

Nomenclature

Vector and matrix notations

x	Scalar notation
$\boldsymbol{x}$	Vector notation
$\boldsymbol{X}$	Matrix notation
$\boldsymbol{\mathcal{X}}$	Tensor notation
$\mathcal{Q}$	Manifold
$T_{\mathcal{Q}}$	Tangent space

Set notations

$\emptyset$	Empty set
$\mathbb{R}$	Set of real numbers
$\mathbb{R}^n$	n-dimensional Euclidean space
$\mathbb{R}_{>0}$	Strictly positive reals
$\mathbb{R}_{\geq 0}$	Positive reals
$\mathbb{N}$	Set of natural numbers
$\mathbb{T}$	Finite time horizon
$\mathbb{X}$	1-dimensional spatial set or domain (*i.e.*, line)
$\mathbb{V}$	3-dimensional spatial set or domain (*i.e.*, volume)

Groups

id	Identity
SO(3)	Lie group of rotations on $\mathbb{R}^3$ (*i.e.*, special orthonormal matrices)
SE(3)	Lie group of homogeneous transformations on $\mathbb{R}^n$
se(3)	Lie algebra of SO(3)
so(3)	Lie algebra of SE(3)

Vector- and matrix operations

$(\cdot)^\top$	Transpose
$(\dot{\cdot})$	First time derivative
$(\ddot{\cdot})$	Second time derivative
$(\hat{\cdot}),(\cdot)^\wedge$	Isomorphism from $\mathbb{R}^6 \to \mathrm{se}(3)$
$(\check{\cdot}),(\cdot)^\vee$	Isomorphism from $\mathrm{se}(3) \to \mathbb{R}^6$
$(\cdot)^\circ$	Reference or rest configuration
$(\cdot)^\star$	Optimal solution
$(\cdot)^{-1}$	Square matrix inverse
$(\cdot)^\dagger$	Moore-Penrose pseudo inverse
$(\cdot)^+$	Generalized matrix inverse
$(\cdot)^\perp$	Annihilator

Operators and letter-like symbols

δ	Variation of a field
∂	Boundary of a set
int	Interior of a set
$\sup_t$	Supremum over continuous time t
dim	Dimension of vector
trace	Trace of matrix
diag	Diagonal of matrix
$\|\cdot\|_{\mathrm{ma}}$	Mean absolute norm
$\|\cdot\|_{\mathrm{rms}}$	Root-mean-square norm

Acronyms

CoM	Center of mass
CoR	Coefficient of restitution
FEM	Finite element method (or model)
ODE	Ordinary differential equation
PDE	Partial differential equation
PneuNet	Pneumatic network
SRM	Soft robotic manipulator
TopoOpt	Topology Optimization

Contents

I

Opening

1

Soft Robots – a new perspective on biomimicry

II

Design of Soft Robots

2

Optimal Design of Soft Robots – a Gradient-based Approach

III

Modeling of Soft Robots

3

Dynamic Modeling – The Constant Strain Approach

Abstract - In this chapter, the continuum dynamics of the soft robot are derived through the differential geometry of spatial curves, which are then related to Finite-Element data to capture the intrinsic geometric and material nonlinearities. To accelerate numerical simulation, a reduced-order integration scheme is introduced to compute the dynamic Lagrangian matrices efficiently. This, in turn, allows for real-time (multi-link) models with sufficient numerical precision. By exploring the passivity and using the parametrization of the hyper-elastic model, we propose a passivity-based adaptive controller that enhances robustness towards material uncertainty and unmodeled dynamics – slowly improving their estimates online. As a study case, a fully 3D-printed soft robot manipulator is developed, which shows good correspondence with the dynamic model under various conditions, *e.g.*, natural oscillations, forced inputs, and subjected to external disturbances like tip-loads. The solidity of the approach is demonstrated through extensive simulations, numerical benchmarks, and experimental validations.

A detailed list of the differences between this chapter and the article on which it is based is provided in the '*Modifications*' chapter of this thesis. Original work is found at [1]

4

Dynamic modeling – Beyond the Constant Strain Approach

Abstract - In this chapter, we address some of the limitation of the previous *Piecewise-Constant-Curvature* (PCC) model presented in Chapter 3, in particular the infinite-dimensionality of the soft robot's deformable body. The continuous dynamics of the soft robot are modeled through the differential geometry of Cosserat beams. Contrary to the PCC model, a wide variety of spatial discretization can be used that better respect the spatial continuity and continuum mechanics of the system. Using a finite-dimensional truncation, the infinite-dimensional system can be written as a reduced-order port-Hamiltonian (pH) model that preserves desirable passivity conditions. Then, a model-based controller is introduced that produces a local minimizer of closed-loop potential energy for the desired end-effector configuration. The stabilizing control utilizes an energy-based approach and exploits the passivity of soft robotic system. The effectiveness of the controller is demonstrated through extensive simulations of various soft manipulators that share a resemblance with biology.

A detailed list of the differences between this chapter and the article on which it is based is provided in the '*Modifications*' chapter of this thesis. Original work is found at [2]. Last modified on July 4, 2022.

4.1   Introduction

The field of soft robotics is slowly growing as a prominent successor to conventional rigid robotics. Contrary to rigid robots, soft robots explore '*soft materials*' that significantly enhance the robot's dexterity, inherent safety, enable a rich family of motion primitives, and provide environmental robustness. By fully exploiting soft materials, soft robotics places the first steps towards achieving performance similar to biology [3–5]. In this work, we primarily focus on a subclass of soft robots called '*soft manipulators*'.

Although significant steps have been taken towards bridging biology and soft robotics, its innate infinite-dimensionality poses substantial challenges on modeling and control. To be more specific, soft robots theoretical allow for infinitely many degrees-of-freedom along their continuously deformable body. This renders them particularly suited for PDE models [6–8] rather than the conventional ODE for traditional robotics [9, 10]. Additionally, their actuation often employs distributed loads (*e.g.*, pneumatics [4, 5] and tendons [8, 11]). Consequently, classical descriptions of rigid links and joints paired with local actuation are no longer viable nor physically representative. This paradigm shift calls for novel control-oriented modeling approaches tailored for hyper-flexible and under-actuated robots.

In the last decade, the field of modeling for soft robotic systems has matured sufficiently and currently their applicability in model-based control is slowly feasible [12]. To highlight a few: reduced-order finite element models [6, 8, 13], constant and non-constant curvature approaches [14, 15], Cosserat-beam models [16, 17], and learning-based approaches [18]. The Piece-wise Constant Curvature (PCC) model – a popular method of state reduction that assumes piecewise constant strains along the soft robot's body – has proven to be viable for modeling solution applicable to feedforward controllers [4], and more recently model-based feedback controllers [14, 15]. Nevertheless, the PCC approach has (severe) limitations. They do not originate from continuum mechanics and thus are only applicable in restrictive settings. Although computationally performance might surpass continuous models, due to intrinsic kinematic restrictions, they are unable to capture important continuum phenomena, like buckling, environmental interaction, or wave propagation.

On the contrary, Cosserat beam-models have shown to capture a wide range of continuum deformations. Cosserat models originate from continuum mechanical PDE description and thus allow a more accurate description of the hyper-flexible nature under large deformations. The computational dynamics of Cosserat beams have been extensively developed by [19] through Geometrically-Exact finite elements on the Lie group SE(3); and recently, these models are slowly gaining popularity in the soft robotics community [11, 16, 17, 20]. Ultimately, the strong nonlinearities paired with the diligence to achieve biological performance encour-

ages Cosserat models for control. Yet, compared to the abundance of PCC soft robotic models, literature on model-based control is scarce.

In this chapter, we aim to highlight the capabilities of Cosserat models for model-based control, in particular energy-based strategies. To this end, a finite-dimensional modeling approach is proposed such that the continuous dynamics can be cast into a port-Hamiltonian (pH) structure. The Lagrangian modeling framework is adopted from [17] and [16], but modified to suit a pH-structure. The main advantage of pH systems is the common formalism with energy-based control. Through the pH structure, we propose an energy-shaping control law that ensures stabilization of the end-effector of the soft robot. Similar energy-based control strategies can be found in [21–24] for rigid-body systems. As a study case, we consider a soft robot manipulator inspired by an octopus tentacle (see Figure 1). With the ability to deform continuously and its distributed muscular system, it is ideal for illustrating the complex morphological motions present in soft robotics. Again, all code is made publicly available under the `SOROTOKI` toolkit on [25], which builds upon previous work Caasenbrood et al. (2021, [2]).

The chapter is organized as follows. Section 4.2 will detail a modeling approach for a general class of soft robot manipulators, starting with the Cosserat-beam theory. In Section 4.3, we propose an energy-shaping control strategy. Lastly, we show the effectiveness of energy-based controller through numerical simulation in Section 4.4, followed by a brief conclusion in Section 4.5.

4.2   Generalized models for soft manipulators

Throughout this work, we will explore Lie group theory. We introduce the following notations: the Lie group of rigid-body transformation on $\mathbb{R}^3$ is denoted by SE(3), whereas the group of homogeneous rotation is denoted by SO(3). The tangent space at the identity of the group is called the Lie algebra, and it can be used to describe the evolution of the Lie group. The Lie algebra of SE(3) and SO(3) are denoted by se(3) and so(3), respectively. Lastly, the cross operator (*i.e.*, "×") and hat operator (*i.e.*, "∧") are used to transform a column vector of $\mathbb{R}^3$ or $\mathbb{R}^6$ into an element of the Lie algebra so(3) or se(3), respectively. A comprehensive introduction is given in Appendix 4.A.1 based on the work of Bullo (1995, [26]).

4.2.1   Preliminary on geometric Cosserat theory

In Cosserat theory, slender deformable solids are modeled as elastic strings subjected to geometric finite-strain theory. Drawing the analogy to soft robotics, we model the soft robot as a one-dimensional spatial curve passing through the geometric center of the soft robot (see Figure 1). Given its spatial-temporal nature, we introduce a temporal variable $t \in [0, T]$ with finite horizon time T, and
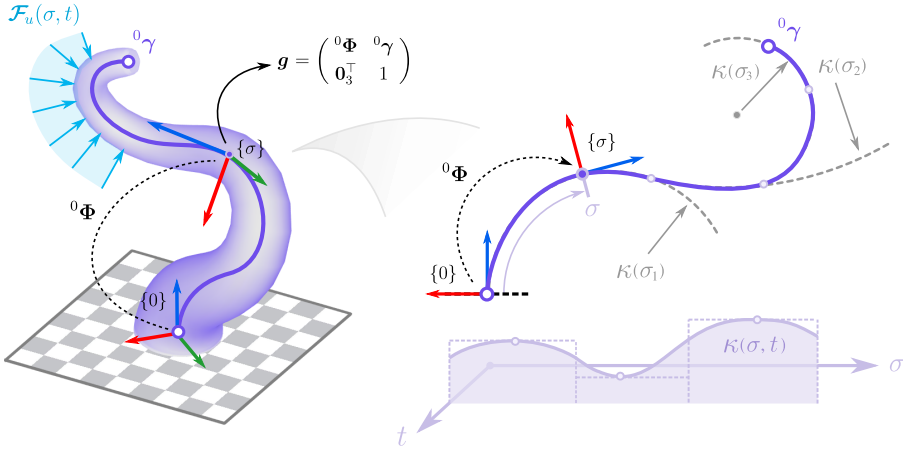
Figure 4.1. Schematic representation of the continuously variable Cosserat beam model for a general class of soft manipulators, given by a backbone $^0\boldsymbol{\gamma} : \mathbb{X} \times \mathbb{T} \to \mathbb{R}^3$ and orientation matrix $^0\boldsymbol{\Phi} : \mathbb{X} \times \mathbb{T} \to \mathrm{SO}(3)$. This forms a parameterized curve $\boldsymbol{g} = (^0\boldsymbol{\Phi}, {}^0\boldsymbol{\gamma}) \in \mathrm{SE}(3)$. The representation of the soft robot is inspired by the octopus' tentacle whose the muscle forces are modelled as a distributed input $\boldsymbol{\mathcal{F}}_u : \mathbb{X} \times \mathbb{T} \to \mathrm{se}^*(3)$ (*i.e.*, a co-vector belonging to the dual space of se(3)).

a spatial variable $\sigma \in [0, L]$ with L the undeformed length of the soft robot. For each point on the backbone, we introduce a (mobile) coordinate frame. The homogeneous rotation related to these coordinate frames is given by the rotation matrix $\boldsymbol{\Phi} : [0, L] \times [0, t] \to \mathrm{SO}(3)$, and their origin by the position vector $\boldsymbol{\gamma} : [0, L] \times [0, T] \to \mathbb{R}^3$. For convenience and readability, we will denote the temporal and spatial domains as $\mathbb{T} = [0, T]$ and $\mathbb{X} = [0, L]$, respectively.

Following the geometric approach [16, 17, 19, 20, 27], we may equivalently represent each coordinate frames that are rigidly attached to the continuous backbone of the soft robot by a parameterized space curve in SE(3):

$$\boldsymbol{g}(\sigma, t) = \begin{pmatrix} \boldsymbol{\Phi}(\sigma, t) & \boldsymbol{\gamma}(\sigma, t) \\ \mathbf{0}_3^\top & 1 \end{pmatrix} \in \mathrm{SE}(3). \tag{4.1}$$

Now, an expression for the strain field $\boldsymbol{\xi}$ and velocity field $\boldsymbol{\eta}$ anywhere on the Cosserat beam can be found by exploring the differential geometry of the curve. To do so, we must introduce some smoothness conditions.

Assumption 4.1 (On differentiability)**.** All control inputs acting on the continuum time-variant system, *i.e.*, a distributed control wrench $\boldsymbol{\mathcal{F}}_u(\sigma, t)$ acting on the backbone curve (4.1), are considered to be sufficiently smooth for any instance $t \in \mathbb{T}$ and $\sigma \in \mathbb{X}$ such that parametrized backbone $\boldsymbol{g}(\sigma, t) \in \mathrm{SE}(3)$ is everywhere differentiable on $\mathbb{X}$ and $\mathbb{T}$.

4.2.2 Local strain and velocity

Following the works of Boyer et al. (2021, [17]) and Renda et al. (2020, [16, 20]), let $\boldsymbol{\Gamma} = (\kappa_1,\,\kappa_2,\kappa_3)^\top$ and $\boldsymbol{U} = (\nu_1,\,\nu_2,\,\nu_3)^\top$ be the torsion-curvature and elongation-shear strain vector, respectively. Then, an expression for strain field $\boldsymbol{\xi}(\sigma,t)$ is obtained through spatial differentiation of $\boldsymbol{g}$:

$$\hat{\boldsymbol{\xi}} := \boldsymbol{g}^{-1}\frac{\partial \boldsymbol{g}}{\partial \sigma} = \begin{pmatrix} \boldsymbol{\Gamma}^\times & \boldsymbol{U} \\ \boldsymbol{0}_3^\top & 0 \end{pmatrix} \implies \boldsymbol{\xi} := \begin{pmatrix} \boldsymbol{\Gamma} \\ \boldsymbol{U} \end{pmatrix}. \tag{4.2}$$

Similarly, let $\boldsymbol{\Omega} = (\omega_1,\omega_2,\omega_3)^\top$ and $\boldsymbol{V} = (v_1,\,v_2,\,v_3)^\top$ be the angular and linear velocity vector, respectively. Then, an expression for velocity field $\boldsymbol{\eta}(\sigma,t)$ is obtained through time differentiation of $\boldsymbol{g}$:

$$\hat{\boldsymbol{\eta}} := \boldsymbol{g}^{-1}\frac{\partial \boldsymbol{g}}{\partial t} = \begin{pmatrix} \boldsymbol{\Omega}^\times & \boldsymbol{V} \\ \boldsymbol{0}_3^\top & 0 \end{pmatrix} \implies \boldsymbol{\eta} := \begin{pmatrix} \boldsymbol{\Omega} \\ \boldsymbol{V} \end{pmatrix}. \tag{4.3}$$

Let it be clear to the reader that $\boldsymbol{\xi}(\sigma,t)$ and $\boldsymbol{\eta}(\sigma,t)$ are yet unknown vector fields, which simply follow from the differential geometry of SE(3), and thus they live in its tangent space se(3) – called its Lie algebra. Now given this geometric structure, we can start detailing the forward kinematics of the soft robot by exploring the smoothness in both space and time of the parameterized curve $\boldsymbol{g}(\sigma,t)$.

Recalling Assumption 4.1, which assumes the configuration space $\boldsymbol{g}$ to be everywhere differentiable, we can introduce the equality of mixed partials, *i.e.*, $\frac{\partial}{\partial t}(\frac{\partial \boldsymbol{g}}{\partial \sigma}) = \frac{\partial}{\partial \sigma}(\frac{\partial \boldsymbol{g}}{\partial t})$. Then, by substitution of $\frac{\partial \boldsymbol{g}}{\partial t} = \boldsymbol{g}\hat{\boldsymbol{\eta}}$ and $\frac{\partial \boldsymbol{g}}{\partial \sigma} = \boldsymbol{g}\hat{\boldsymbol{\xi}}$, we obtain the so-called '*compatibility equation*':

$$\boldsymbol{g}\hat{\boldsymbol{\eta}}\hat{\boldsymbol{\xi}} + \boldsymbol{g}\frac{\partial \hat{\boldsymbol{\xi}}}{\partial t} = \boldsymbol{g}\hat{\boldsymbol{\xi}}\hat{\boldsymbol{\eta}} + \boldsymbol{g}\frac{\partial \hat{\boldsymbol{\eta}}}{\partial \sigma}, \tag{4.4}$$

which can be regarded as an equality constraint that follows from the smoothness of the group (or manifold) in both space and time. Pre-multiplying the expression above with $\boldsymbol{g}^{-1} \in$ SE(3) and rearranging the equality, we obtain

$$\frac{\partial \hat{\boldsymbol{\eta}}}{\partial \sigma} = -\left(\hat{\boldsymbol{\xi}}\hat{\boldsymbol{\eta}} - \hat{\boldsymbol{\eta}}\hat{\boldsymbol{\xi}}\right) + \dot{\hat{\boldsymbol{\xi}}}. \tag{4.5}$$

Focusing on the RHS term $(\hat{\boldsymbol{\xi}}\hat{\boldsymbol{\eta}} - \hat{\boldsymbol{\eta}}\hat{\boldsymbol{\xi}})$, we can recognize the Lie bracket or the commuter between the geometric vector fields $\boldsymbol{\xi}$ and $\boldsymbol{\eta}$ (see [10]). Since the Lie bracket $[\hat{\boldsymbol{\xi}}, \hat{\boldsymbol{\eta}}]$ itself also belongs to Lie algebra se(3), which is isomorphic to $\mathbb{R}^6$ via the operator $\hat{\boldsymbol{\eta}} \to \boldsymbol{\eta}$, we can rewrite the expressions as follows

$$\frac{\partial \boldsymbol{\eta}}{\partial \sigma} = -\mathbf{ad}_{\boldsymbol{\xi}}\boldsymbol{\eta} + \dot{\boldsymbol{\xi}}, \tag{4.6}$$

where $\mathbf{ad}_{(\cdot)} : \mathbb{R}^6 \to \mathbb{R}^{6\times 6}$ defines the adjoint action on vectors belonging to the Lie algebra se(3). Drawing an analogy to rigid robotics, the expression in (4.6) may be seen as the forward velocity kinematics for a serial chain robot manipulator with infinitely many links. To that end, we reformulate (4.2), (4.6) and the time derivative of (4.6) (*i.e.*, the acceleration) as a system of PDEs describing the full continuum-body kinematics of the continuum body:

$$\frac{\partial}{\partial\sigma}\begin{pmatrix} \boldsymbol{g} \\ \boldsymbol{\eta} \\ \dot{\boldsymbol{\eta}} \end{pmatrix} = \begin{pmatrix} \boldsymbol{g}\hat{\boldsymbol{\xi}} \\ -\mathbf{ad}_{\xi}\boldsymbol{\eta} + \dot{\boldsymbol{\xi}} \\ -\mathbf{ad}_{\dot{\xi}}\dot{\boldsymbol{\eta}} - \mathbf{ad}_{\xi}\dot{\boldsymbol{\eta}} + \ddot{\boldsymbol{\xi}} \end{pmatrix}. \tag{4.7}$$

For a general case, the boundary conditions of PDE in (4.7) should satisfy $\boldsymbol{g}(0,t) = \boldsymbol{g}_0$, $\boldsymbol{\eta}(0,t) = \boldsymbol{\eta}_0$ and $\dot{\boldsymbol{\eta}}(0,t) = \dot{\boldsymbol{\eta}}_0$. However, in case of a manipulator whose base is spatially fixed, the boundary conditions should satisfy $\boldsymbol{g}(0,t) = g_0$, and $\boldsymbol{\eta}(0,t) = \dot{\boldsymbol{\eta}}(0,t) = \mathbf{0}_6$. Notice that if the strain fields $\boldsymbol{\xi}$, $\dot{\boldsymbol{\xi}}$, and $\ddot{\boldsymbol{\xi}}$ are known, the partial differential equation in (4.7) can simply be treated as a system of ODEs, which can be easily solved using numerical approaches.

4.2.3   Finite-dimensional projection

Similar to finite element methods, we wish to find a finite-dimensional approximation of the strain field $\boldsymbol{\xi}(\sigma,t)$ for all points on the material domain $\mathbb{X}$. To do so, we assume the following:

Assumption 4.2. Assuming the strain field has a separable spatio-temporal nature, any entry of the strain vector field $\boldsymbol{\xi} = (\xi_1, \xi_2, ..., \xi_6)^\top$ can be written as an infinite expansion of the following form:

$$\xi_i(\sigma,t) = \sum_{n=1}^{\infty} \theta_n(\sigma) q_{i,n}(t) + \xi_i^{\circ}(\sigma) \quad i \in \{1, \ldots, 6\}, \tag{4.8}$$

where $\{\theta_n\}_{n=1}^{\infty}$ is the set of (orthogonal) basis functions $\theta_n : \mathbb{X} \to \mathbb{R}$ together with modal coefficients $q_{i,n} : \mathbb{T} \to \mathbb{R}$, and an intrinsic time-invariant strain $\xi_i^{\circ} : \mathbb{X} \to \mathbb{R}$. The basis functions $\theta_n(\cdot)$ and the modal coefficients $q_n(\cdot)$ are both smooth functions.

Assumption 4.3. Given infinite expansion (4.8), the k-th order truncation for any entry of the strain field, defined as

$$[\xi_i]_k(\sigma,t) := \sum_{n=1}^{k} \theta_n(\sigma) q_{i,n}(t) + \xi_i^{\circ}(\sigma) \quad i \in \{1, \ldots, 6\}, \tag{4.9}$$

converges uniformly on $\mathbb{X}$ and $\mathbb{T}$ as the index $k \to \infty$. Moreover, we assume that uniform convergence holds for its partial derivatives $\frac{\partial}{\partial t}[\boldsymbol{\xi}]_k$ and $\frac{\partial}{\partial\sigma}[\boldsymbol{\xi}]_k$.
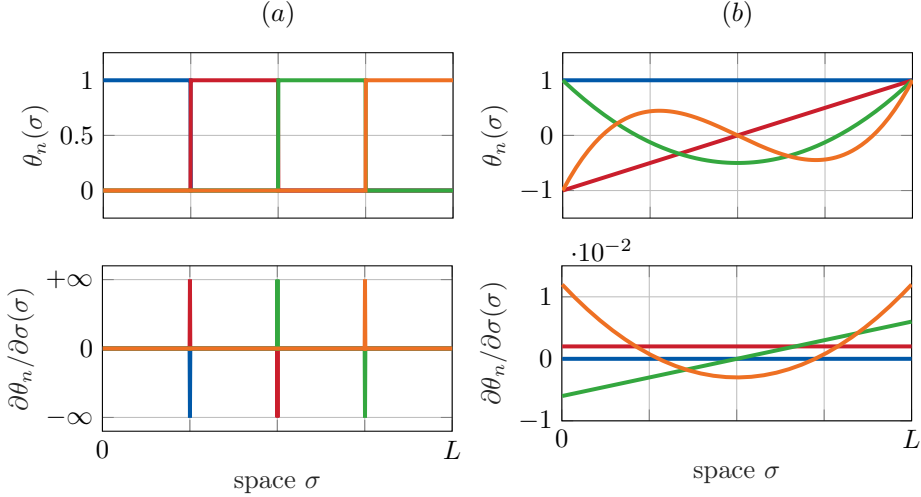
Figure 4.2. Example plot of the Constant-Strain parameterization in Chapter 3 (*a*), and the new strain parameterization (4.12) using Chebyshev polynomials (*b*). The ordering of the strain basis is as follows $\{\theta_1, ..., \theta_4\} = \{$ —, —, —, — $\}$. Notice that the discontinuities in the PCC models induce spikes that directly violate the compatibility equation in (4.4).

Accordingly, we can rewrite the k-th order truncation of the complete strain field as a linear matrix operation as follows

$$[\boldsymbol{\xi}]_k = \left(\boldsymbol{I}_6 \otimes \begin{bmatrix} \theta_1 & \cdots & \theta_k \end{bmatrix} \right) \boldsymbol{q} + \boldsymbol{\xi}^\circ, \tag{4.10}$$

$$= \underbrace{\begin{pmatrix} \theta_1 & \cdots & \theta_k & \cdots & 0 & \cdots & 0 \\ \vdots & \ddots & \vdots & \ddots & \vdots & \vdots & \vdots \\ 0 & \cdots & 0 & \cdots & \theta_1 & \cdots & \theta_k \end{pmatrix}}_{\boldsymbol{\Theta}(\sigma)} \underbrace{\begin{pmatrix} q_{1,1} \\ \vdots \\ q_{6,k} \end{pmatrix}}_{\boldsymbol{q}(t)} + \boldsymbol{\xi}^\circ, \tag{4.11}$$

where $\boldsymbol{\Theta} \in \mathbb{R}^{6 \times 6k}$ is a sparse matrix-valued function whose columns are mutually orthonormal, the operator $\otimes$ denotes the Kronecker product, and the vector $\boldsymbol{q} \in \mathbb{R}^{6k}$ the collection of all time-variant modal coefficients related to the columns of $\boldsymbol{\Theta}$. Although a wide variety of bases are possible (see for instance [15, 17]), we have chosen a modified Legendre polynomial set:

$$\theta_n(\sigma) = \frac{2}{2^n(n-1)!} \frac{d^{n-1}}{d\sigma^{n-1}} \left[\left(\frac{2\sigma}{L} - 1 \right)^2 - 1 \right]^{n-1} \tag{4.12}$$

with $n \in \mathbb{Z}/\{0\}$ the polynomial degree. A comparison between the proposed basis and previous method in Chapter 3 is shown in Figure 4.2. Please note

now that the inner product between elements of the set of modified Legendre functionals $\{\theta_n\}_{n=1}^k$ satisfies $\langle\theta_i, \theta_j\rangle_{\mathbb{X}} := \int_{\mathbb{X}} \theta_i\theta_j d\sigma = 0$ for $i \neq j$, and 1 otherwise. An alternative option could be constructing the set of basis functions through the so-called 'snapshot decomposition method' using FEM-driven data [6, 7, 28].

Remark 4.1. *The idea of joint parameterization by investigating the relation between material and structural topology of the soft robot is explored in Chapter 5.*

4.2.4   Reduced-order curve kinematics

Given the finite-dimensional truncation in (4.11), we can now find an expression for the finite-dimensional forward kinematics in terms of the generalized coordinates $\boldsymbol{q}$ and its velocities components $\dot{\boldsymbol{q}}$.

First, let us regard the configuration of the soft robot $\boldsymbol{g} \in \mathrm{SE}(3)$. Recall that the spatial evolution of the curve is described by $\partial\boldsymbol{g}/\partial\sigma = \boldsymbol{g}\boldsymbol{\xi}^\wedge$, see Eq. (4.2). Given the initial condition $\boldsymbol{g}(0,\cdot) = \boldsymbol{g}_0$, an approximation of the continuously deformable soft robot can be obtained by partial integration over the spatial domain:

$$[\boldsymbol{g}]_k(\sigma, \boldsymbol{q}) = \boldsymbol{g}_0 \exp_{\mathrm{SE}(3)} \left[\int_0^\sigma [\hat{\boldsymbol{\xi}}]_k(s, \boldsymbol{q}) \, ds \right]. \tag{4.13}$$

The computation of the mapping $\exp_{\mathrm{SE}(3)}$ is given in Appendix 4.A.1. Please note that this nothing more than the reconstruction of the curve by integration of its tangent space along its spatial parameter σ. Next, lets regard the velocity kinematics $\boldsymbol{\eta}(\sigma, t)$ for any point σ on the backbone curve. Using the differential property of the adjoint action $\mathbf{ad}_{\boldsymbol{\xi}} = -\partial/\partial\sigma[\mathbf{Ad}_{g^{-1}}]\mathbf{Ad}_g$ [10], we can rewrite the continuous forward kinematics in (4.6) as

$$\frac{\partial\boldsymbol{\eta}}{\partial\sigma} = \frac{\partial}{\partial\sigma} \left(\mathbf{Ad}_{g^{-1}} \right) \mathbf{Ad}_g \boldsymbol{\eta} + \dot{\boldsymbol{\xi}}. \tag{4.14}$$

Now, given the initial condition $\boldsymbol{\eta}(0, t) = \mathbf{0}_6$ and the approximations $[\boldsymbol{\xi}]_k$ and $[\boldsymbol{g}]_k$, we can find an approximation to the velocity twist $\boldsymbol{\eta}$ by partial integration over space:

$$[\boldsymbol{\eta}]_k(\sigma, \boldsymbol{q}, \dot{\boldsymbol{q}}) = \mathbf{Ad}_{[\boldsymbol{g}]_k}^{-1} \int_0^\sigma \mathbf{Ad}_{[\boldsymbol{g}]_k} \boldsymbol{\Theta} \, ds \, \dot{\boldsymbol{q}} := [\boldsymbol{J}]_k \, \dot{\boldsymbol{q}}, \tag{4.15}$$

which naturally gives rise to the geometric Jacobian $[\boldsymbol{J}]_k \in \mathbb{R}^{6 \times 6k}$. The geometric Jacobian plays an important role in obtaining the Lagrangian form of the reduced-order dynamic model. Finally, to express the acceleration twist, we take the time-derivative of (4.15) leading to

$$\begin{aligned}
[\dot{\boldsymbol{\eta}}]_k &= [\boldsymbol{J}]_k\ddot{\boldsymbol{q}} + [\dot{\boldsymbol{J}}]_k\dot{\boldsymbol{q}}, \\
&= [\boldsymbol{J}]_k\ddot{\boldsymbol{q}} + \mathbf{Ad}_{[\boldsymbol{g}]_k}^{-1} \int_0^\sigma \mathbf{Ad}_{[\boldsymbol{g}]_k} \mathbf{ad}_{[\boldsymbol{\eta}]_k} \boldsymbol{\Theta} \, ds \, \dot{q},
\end{aligned} \tag{4.16}$$

which gives rise to the analytic expression of the time-derivative of the geometric Jacobian $[\dot{\boldsymbol{J}}]_k$ (see Appendix 4.A.2 for the derivation).

4.2.5   Reduced-order curve dynamics using Newton-Euler

Here, we detail the dynamics of the Cosserat beam. A majority of the dynamic framework presented here is adopted from Boyer et al. (2021, [17]); yet we introduce some modification to allow a pH-structure. First, let us consider an infinitesimal slice of continuum body that is perpendicular to the backbone curve. The kinetic momenta of this infinitesimal slice is then given by $\boldsymbol{\mu}(\sigma, t) := \boldsymbol{\mathcal{M}}\boldsymbol{\eta}(\sigma, t)$ in which $\boldsymbol{\mathcal{M}} \in \mathrm{se}^*(3) \times \mathrm{se}(3) \cong \mathbb{R}^{6 \times 6}$ denotes the symmetric inertia tensor.

Remark 4.2. *For some soft robots, the inertia tensor $\boldsymbol{\mathcal{M}}$ may have an explicit dependency on space or time (or both). Nevertheless, for sake of simplicity, we limit ourselves to a diagonal invariant inertia tensor:*

$$\boldsymbol{\mathcal{M}}(\sigma, t) \cong \boldsymbol{\mathcal{M}} = \begin{pmatrix} \rho_0 \boldsymbol{\mathcal{J}} & \mathbf{0}_{3 \times 3} \\ \mathbf{0}_{3 \times 3} & \rho_0\, A \boldsymbol{I}_3 \end{pmatrix} \succ 0,$$

in which the (cross-sectional average) density is $\rho_0 > 0$, the cross-sectional area of the soft robot by $A > 0$, and the second moment of area $\boldsymbol{\mathcal{J}} \in \mathrm{so}^*(3) \times \mathrm{so}(3) \cong \mathbb{R}^{3 \times 3}$.

Using the expression of the kinetic momenta $\boldsymbol{\mu}(\sigma, t)$ of the infinitesimal rigid body in free-motion, we can write the equation of motion for a particular slice at σ using the Newton-Euler equations:

$$\frac{\partial}{\partial t}(\mathbf{Ad}_{\boldsymbol{g}}^{-\top} \boldsymbol{\mu}) = \mathbf{Ad}_{g}^{-\top} \boldsymbol{\mathcal{F}}, \tag{4.17}$$

where again $\mathbf{Ad}_{(.)}$ stands for the adjoint action, and $\boldsymbol{\mathcal{F}} = \boldsymbol{\mathcal{F}}_c + \boldsymbol{\mathcal{F}}_u - \boldsymbol{\mathcal{F}}_{\mathrm{g}} - \boldsymbol{\mathcal{F}}_{\mathrm{e}}$ the resultant wrench that is composed of the constraint wrench $\boldsymbol{\mathcal{F}}_c$, the input wrench $\boldsymbol{\mathcal{F}}_u$, and the potential wrenches due to gravity and visco-elasticity, $\boldsymbol{\mathcal{F}}_{\mathrm{g}}$ and $\boldsymbol{\mathcal{F}}_{\mathrm{e}}$, respectively. Further evaluation of (4.17) leads to

$$\boldsymbol{\mathcal{M}}\dot{\boldsymbol{\eta}} - \mathbf{ad}_{\boldsymbol{\eta}}^{\top} \boldsymbol{\mathcal{M}}\boldsymbol{\eta} = \boldsymbol{\mathcal{F}}, \tag{4.18}$$

where we used the fact that $\dot{\mathbf{Ad}}_{\boldsymbol{g}}^{-1} = -\mathbf{ad}_{\boldsymbol{\eta}} \mathbf{Ad}_{\boldsymbol{g}^{-1}}$. Before continuing, we introduce a slight modification to the relation above. Using the fact that $\mathbf{ad}_{\boldsymbol{\eta}}\boldsymbol{\eta} = \mathbf{0}_6$, we can introduce the vector $\boldsymbol{\mathcal{M}}\mathbf{ad}_{\boldsymbol{\eta}}\boldsymbol{\eta}$ to (4.18) without affecting the dynamics. The importance of this modification originates from the preservation of passivity in the Lagrangian model, which is an important property in stability theorems for robotics. By substitution of the null vector, the equation of motion becomes

$$\boldsymbol{\mathcal{M}}\dot{\boldsymbol{\eta}} + \left(\boldsymbol{\mathcal{M}}\mathbf{ad}_{\boldsymbol{\eta}} - \mathbf{ad}_{\boldsymbol{\eta}}^{\top} \boldsymbol{\mathcal{M}}\right) \boldsymbol{\eta} = \boldsymbol{\mathcal{F}}, \tag{4.19}$$

which is nothing more than the Newton-Euler equation for rigid-body motion on $\mathbb{R}^3$. To introduce the (reduced-order) Cosserat kinematics and make the expression symmetric, we substitute (4.15) and (4.16) into (4.19) and pre-multiply by $[\boldsymbol{J}]_k^\top$:

$$[\boldsymbol{J}]_k^\top \left(\boldsymbol{\mathcal{M}}[\boldsymbol{J}]_k \ddot{\boldsymbol{q}} + \boldsymbol{\mathcal{M}}[\dot{\boldsymbol{J}}]_k \dot{\boldsymbol{q}} + \boldsymbol{\mathcal{C}}_{[\boldsymbol{\eta}]_k} \dot{\boldsymbol{q}} \right) = [\boldsymbol{J}]_k^\top \left(\boldsymbol{\mathcal{F}}_u - \boldsymbol{\mathcal{F}}_g - \boldsymbol{\mathcal{F}}_e \right), \quad (4.20)$$

where $\boldsymbol{\mathcal{C}}_{(\cdot)} = -\boldsymbol{\mathcal{C}}_{(\cdot)}^\top := \boldsymbol{\mathcal{M}} \mathbf{ad}_{(\cdot)} - \mathbf{ad}_{(\cdot)}^\top \boldsymbol{\mathcal{M}}$ is a skew-symmetric matrix. It is important to note that by pre-multiplication of the transpose Jacobian, we have eliminated the constraint wrenches, *i.e.*, $[\boldsymbol{J}]_k^\top \boldsymbol{\mathcal{F}}_c = \boldsymbol{0}_n$ [10]. Finally, the finite-dimensional dynamics of the deformable soft robot is found by spatial integration of (4.20) over the material domain $\mathbb{X}$. The overall dynamics can be written in familiar Euler-Lagrangian (EL) form as follows

$$\boldsymbol{M}(\boldsymbol{q})\ddot{\boldsymbol{q}} + \boldsymbol{C}(\boldsymbol{q}, \dot{\boldsymbol{q}})\dot{\boldsymbol{q}} + \boldsymbol{f}_g(\boldsymbol{q}) + \boldsymbol{f}_e(\boldsymbol{q}, \dot{\boldsymbol{q}}) = \boldsymbol{\tau}(\boldsymbol{q}, \boldsymbol{u}) \quad (4.21)$$

with the system matrices:

$$\boldsymbol{M}(\boldsymbol{q}) = \int_{\mathbb{X}} [\boldsymbol{J}]_k^\top \boldsymbol{\mathcal{M}}[\boldsymbol{J}]_k \, d\sigma, \quad (4.22)$$

$$\boldsymbol{C}(\boldsymbol{q}, \dot{\boldsymbol{q}}) = \int_{\mathbb{X}} [\boldsymbol{J}]_k^\top \left(\boldsymbol{\mathcal{M}}[\dot{\boldsymbol{J}}]_k + \boldsymbol{\mathcal{C}}_{[\boldsymbol{\eta}]_k}[\boldsymbol{J}]_k \right) \, d\sigma, \quad (4.23)$$

$$\boldsymbol{f}_g(\boldsymbol{q}) = \int_{\mathbb{X}} [\boldsymbol{J}]_k^\top \boldsymbol{\mathcal{F}}_g \, d\sigma, \quad (4.24)$$

$$\boldsymbol{f}_e(\boldsymbol{q}, \dot{\boldsymbol{q}}) = \int_{\mathbb{X}} [\boldsymbol{J}]_k^\top \boldsymbol{\mathcal{F}}_e \, d\sigma := \boldsymbol{K}\boldsymbol{q} + \boldsymbol{D}\dot{\boldsymbol{q}}, \quad (4.25)$$

$$\boldsymbol{\tau}(\boldsymbol{q}, \boldsymbol{u}) = \int_{\mathbb{X}} [\boldsymbol{J}]_k^\top \boldsymbol{\mathcal{F}}_u \, d\sigma := \boldsymbol{G}\boldsymbol{u}, \quad (4.26)$$

where $\boldsymbol{M}$ is the generalized inertia matrix, $\boldsymbol{C}$ the centripetal-Coriolis matrix, $\boldsymbol{f}_g$ a vector of generalized potential forces with $\boldsymbol{\mathcal{F}}_g = -\mathbf{Ad}_{[\boldsymbol{g}]_k}^\top \boldsymbol{\mathcal{M}} \boldsymbol{a}_g$ the external wrench acting on the body due to gravitational acceleration $\boldsymbol{a}_g$, and $\boldsymbol{\mathcal{F}}_e$ a vector of visco-elastic forces imposed by the stiffness matrix $\boldsymbol{K} \succ 0$ and damping matrix $\boldsymbol{D} \succ 0$. Following the procedures in finite elements and assuming linear visco-elasticity, the stiffness matrix and damping matrix are computed through spatial integration:

$$\boldsymbol{K} = \int_{\mathbb{X}} \boldsymbol{\Theta}^\top \boldsymbol{\mathcal{K}} \boldsymbol{\Theta} \, d\sigma, \quad (4.27)$$

$$\boldsymbol{D} = \int_{\mathbb{X}} \boldsymbol{\Theta}^\top \boldsymbol{\mathcal{D}} \boldsymbol{\Theta} \, d\sigma, \quad (4.28)$$

where $\boldsymbol{\mathcal{K}} \in \mathrm{se}^*(3) \times \mathrm{se}(3)$ and $\boldsymbol{\mathcal{D}} \in \mathrm{se}^*(3) \times \mathrm{se}(3)$ are the stiffness and damping tensor, respectively. The vector $\boldsymbol{G}\boldsymbol{u}$ represents the distributed forces and torques

generated by various kinds of the internal actuators (*e.g.*, tendons or pneumatics). Again, system of matrices can then be efficiently recovered using a Matrix-Differential solver proposed in Chapter 3. If $\text{rank}(\boldsymbol{G}) < \dim(\boldsymbol{q})$, a system is said to be under-actuated. Within the context of soft robotics, whose infinite-dimensional configuration space cannot be matched by a finite number of actuators, these systems are often intrinsically under-actuated.

Lemma 4.1. *The inertia matrix $\boldsymbol{M}(\boldsymbol{q})$ is a symmetric, positive definite, symmetric. and is uniformly bounded such that there exists positive constants $\lambda^- \leq \lambda^+$ such that $\lambda^- \boldsymbol{I}_n \preceq \boldsymbol{M}(\boldsymbol{q}) \preceq \lambda^+ \boldsymbol{I}_n < \infty$.* ▲

Proof. Proof can be found in Spong et al. (2006, [9]). □

Lemma 4.2. *Given the inertia matrix $\boldsymbol{M}(\boldsymbol{q})$ and the Coriolis matrix $\boldsymbol{C}(\boldsymbol{q}, \dot{\boldsymbol{q}})$ as described by* (4.22) *and* (4.23)*, respectively, it can be shown that the matrix $\dot{\boldsymbol{M}} - 2\boldsymbol{C}$ is skew-symmetric.* ▲

Proof. To show $\dot{\boldsymbol{M}} - 2\boldsymbol{C}$ is skew-symmetric, we start by computing the time-derivative of the inertia matrix. For sake of clarity, lets abbreviate the Jacobians matrices $[\boldsymbol{J}]_k = \boldsymbol{J}$ and $[\dot{\boldsymbol{J}}]_k = \dot{\boldsymbol{J}}$. Through chain differentiation, we find

$$\dot{\boldsymbol{M}} = \int_{\mathbb{X}} \dot{\boldsymbol{J}}^\top \boldsymbol{\mathcal{M}} \boldsymbol{J} + \boldsymbol{J}^\top \boldsymbol{\mathcal{M}} \dot{\boldsymbol{J}} \, d\sigma, \tag{4.29}$$

Then, calculating $\dot{\boldsymbol{M}} - 2\boldsymbol{C}$ leads to

$$\dot{\boldsymbol{M}} - 2\boldsymbol{C} = \int_{\mathbb{X}} \dot{\boldsymbol{J}}^\top \boldsymbol{\mathcal{M}} \boldsymbol{J} - \boldsymbol{J}^\top \boldsymbol{\mathcal{M}} \dot{\boldsymbol{J}} - 2\boldsymbol{J}^\top \boldsymbol{\mathcal{C}} \, \boldsymbol{J} \, d\sigma. \tag{4.30}$$

Since the matrix $\boldsymbol{J}^\top \boldsymbol{\mathcal{C}} \boldsymbol{J}$ is skew-symmetric, the remainder of the proof is to show that the matrix $\boldsymbol{S} = \dot{\boldsymbol{J}}^\top \boldsymbol{\mathcal{M}} \boldsymbol{J} - \boldsymbol{J}^\top \boldsymbol{\mathcal{M}} \dot{\boldsymbol{J}}$ also satisfies skew-symmetry. Since the inertia tensor is symmetric $\boldsymbol{\mathcal{M}} = \boldsymbol{\mathcal{M}}^\top$, we can easily show this holds true:

$$\boldsymbol{S} = \dot{\boldsymbol{J}}^\top \boldsymbol{\mathcal{M}}^\top \boldsymbol{J} - \boldsymbol{J}^\top \boldsymbol{\mathcal{M}}^\top \dot{\boldsymbol{J}},$$
$$= - \left(\dot{\boldsymbol{J}}^\top \boldsymbol{\mathcal{M}}^\top \boldsymbol{J} - \boldsymbol{J}^\top \boldsymbol{\mathcal{M}} \dot{\boldsymbol{J}} \right)^\top = -\boldsymbol{S}^\top. \tag{4.31}$$

Therefore, the matrix $\dot{\boldsymbol{M}}(\boldsymbol{q}) - 2\boldsymbol{C}(\boldsymbol{q}, \dot{\boldsymbol{q}})$ is skew-symmetric for all $\boldsymbol{q}, \dot{\boldsymbol{q}} \in \mathbb{R}^n$ □

In literature, Lemma 4.2 is often referred to as the passivity condition [9, 10, 24]. It implies that, in the absence of external dissipation, the total energy of the system (*i.e.*, the Hamiltonian) is conserved. It is also worth mentioning that this condition does not necessarily hold true for all cases, only for particular computations of the Coriolis matrix $\boldsymbol{C}(\boldsymbol{q}, \dot{\boldsymbol{q}})$ (*e.g.*, through the Christoffel symbols).

4.2.6   Port-Hamiltonian formulation

In this section, the Lagrangian model in (4.21) is rewritten in port-Hamiltonian form. To this end, we define the generalized momenta $\boldsymbol{p} := \boldsymbol{M}\dot{\boldsymbol{q}}$. Then, the (reduced-order) Hamiltonian is given by $\mathcal{H}(\boldsymbol{q}, \boldsymbol{p}) := \mathcal{K}(\boldsymbol{q}, \boldsymbol{p}) + \mathcal{U}(\boldsymbol{q})$ with $\mathcal{K} = \frac{1}{2}\boldsymbol{p}^\top \boldsymbol{M}^{-1}\boldsymbol{p}$ and $\mathcal{U}(\boldsymbol{q})$ the kinetic and potential energy, respectively.

Given the system's Hamiltonian $\mathcal{H}$, it can be shown that generalized velocities can be written in terms of partial derivatives of the Hamiltonian function

$$\dot{\boldsymbol{q}} = \nabla_{\boldsymbol{p}}\mathcal{H} \quad \implies \quad \nabla_{\boldsymbol{p}}\mathcal{H} := \left(\frac{\partial \mathcal{H}}{\partial \boldsymbol{p}}\right)^\top = \boldsymbol{M}^{-1}\boldsymbol{p}. \tag{4.32}$$

where we denote $\nabla_{\boldsymbol{x}}(\cdot) := \partial(\cdot)^\top/\partial\boldsymbol{x}$ as the gradient w.r.t. a vector field $\boldsymbol{x}$. Note that $\boldsymbol{M}^{-1}$ is always exists due to the positive definiteness condition in Lemma 4.1. Similarly, we seek a differential description that relates the time evolution of $\boldsymbol{p}$ to a state-derivative of the Hamiltonian function. Applying the chain rule of differentiation to the generalized momenta:

$$\begin{aligned}
\dot{\boldsymbol{p}} &= \dot{\boldsymbol{M}}\dot{\boldsymbol{q}} + \boldsymbol{M}\ddot{\boldsymbol{q}}, \\
&= \left(\dot{\boldsymbol{M}} - \boldsymbol{C} - \boldsymbol{D}\right)\boldsymbol{M}^{-1}\boldsymbol{p} - \boldsymbol{K}\boldsymbol{q} - \boldsymbol{f}_{\mathrm{g}} + \boldsymbol{G}\boldsymbol{u},
\end{aligned} \tag{4.33}$$

Taking the partial derivative of the Hamiltonian $\mathcal{H}$ w.r.t. the generalized coordinates $\boldsymbol{q}$, we find

$$\nabla_{\boldsymbol{q}}\mathcal{H} = \frac{1}{2}\nabla_{\boldsymbol{q}}\left[\dot{\boldsymbol{q}}^\top \boldsymbol{M}(\boldsymbol{q})\dot{\boldsymbol{q}}\right] + \nabla_{\boldsymbol{q}}\mathcal{U}. \tag{4.34}$$

To relate (4.33) and (4.34), we explores some structural properties in the Lagrangian model. To be more specific, we exploit the skew-symmetry condition as detailed in Lemma 4.2. According to the Spong et al. (2006, [9]), if the matrix $\dot{\boldsymbol{M}} - 2\boldsymbol{C}$ satisfies the passivity condition in Lemma 4.2, it can be shown that

$$\left(\dot{\boldsymbol{M}} - 2\boldsymbol{C}\right)\dot{\boldsymbol{q}} = -\nabla_{\boldsymbol{q}}\left[\dot{\boldsymbol{q}}^\top \boldsymbol{M}(\boldsymbol{q})\dot{\boldsymbol{q}}\right] - \dot{\boldsymbol{M}}\dot{\boldsymbol{q}}. \tag{4.35}$$

Finally, by combining (4.32), (4.33), (4.34), and (4.35), we can show that the Lagrangian model in (4.21) can be equivalently rewritten as a standard port-Hamiltonian (pH) system:

$$\Sigma_{\mathrm{beam}} : \begin{cases} \dot{\boldsymbol{q}} &= \nabla_{\boldsymbol{p}}\mathcal{H}, \\ \dot{\boldsymbol{p}} &= -\nabla_{\boldsymbol{q}}\mathcal{H} - \boldsymbol{D}\nabla_{\boldsymbol{p}}\mathcal{H} + \boldsymbol{G}\boldsymbol{u}. \end{cases} \tag{4.36}$$

The advantage of the port-Hamiltonian system Σ_{beam} over the standard EL structure in (4.21), and as also seen in Chapter 3, is the general applicability to different

physical domains and the common formalism with energy-based control, which we will explore further in the next section. By collocating the state variable into a state vector $\boldsymbol{x} = (\boldsymbol{q}^\top, \boldsymbol{p}^\top)^\top$, we may write the system into an equivalent form: $\dot{\boldsymbol{x}} = (\boldsymbol{\mathcal{J}} - \boldsymbol{\mathcal{R}}) \nabla_{\boldsymbol{x}} \mathcal{H}(\boldsymbol{x}) + \boldsymbol{\mathcal{B}}(\boldsymbol{x}) \boldsymbol{u}$, where $\boldsymbol{\mathcal{J}} = -\boldsymbol{\mathcal{J}}^\top$ a skew-symmetric matrix, $\boldsymbol{\mathcal{R}} \succeq 0$ a positive semi-definite dissipation matrix.

4.3 Energy-based controller for tasks on SE(3)

Given the previous reduced-order dynamic model, our objective here is to find a controller $\boldsymbol{u}$ that ensures $\lim_{t \to \infty} \boldsymbol{g}(L, t) = \boldsymbol{g}_d$ in which $\boldsymbol{g}_d \in$ SE(3) denotes the desired configuration of the end-effector. To achieve the control objective, the main idea is to reshape the potential energy function of the reduced-order finite-dimensional system using a standard energy-shaping techniques, common to standard port-controlled Hamiltonian models [22, 23].

We adopted an energy-based control strategy akin to the works of Franco et al. (2020, [21]), Ortega et al. (1988, [23, 24]) and Schaft (2004, [22]). Following the energy-shaping strategy, the model-based nonlinear controller becomes

$$\boldsymbol{u} = \boldsymbol{G}^+ \left(\nabla_{\boldsymbol{q}} \mathcal{H} - \nabla_{\boldsymbol{q}} \mathcal{H}_d \right), \tag{4.37}$$

where $\boldsymbol{G}^+ = \left(\boldsymbol{G}^\top \boldsymbol{G} \right)^{-1} \boldsymbol{G}^\top$ is the generalized inverse of the actuation map $\boldsymbol{G}$, and the desired Hamiltonian in closed loop $\mathcal{H}_d = \frac{1}{2} \boldsymbol{p}^\top \boldsymbol{M}^{-1} \boldsymbol{p} + \mathcal{U}_d$ that satisfies $\text{argmin}_{\boldsymbol{g}_L} \mathcal{U}_d = \boldsymbol{g}_d$ with $\boldsymbol{g}_L = \boldsymbol{g}(L, \cdot)$ the pose of the end-effector. Note that we purposefully omitted any damping injection as the system's intrinsic visco-elastic damping is deemed sufficiently large to guarantee stability. Following the concept of a kinematic feedback controller [17, 26] that artificially mimic an elastic element between the end-effector and the desired configuration in SE(3), we have choose the gradient of the desired potential energy as

$$\nabla_{\boldsymbol{q}} \, \mathcal{U}_d = \lambda_1 \boldsymbol{J}^\top \left(\boldsymbol{J} \boldsymbol{J}^\top + \lambda_2 \boldsymbol{I} \right)^{-1} \boldsymbol{\mathcal{F}}_u, \tag{4.38}$$

where $\lambda_1 > 0$ is a proportional gain, $\lambda_2 > 0$ a controller gain related to the artificial damping of the pseudo-inverse, $\boldsymbol{\mathcal{F}}_u = k_p T_{SE(3)}(\boldsymbol{\mathcal{E}})\boldsymbol{\mathcal{E}}$ an artificial control wrench with positive definite stiffness matrix k_p, $\boldsymbol{\mathcal{E}} = \log_{\text{SE}(3)}([\boldsymbol{g}_L]_k^{-1} \boldsymbol{g}_d)$ where $\log_{\text{SE}(3)}(\cdot)$ and $T_{\text{SE}(3)}(\cdot)$ denote the logarithmic map (see Appendix 4.A.1) and the tangent-space map, respectively. We refer the reader to Sonneville et al. (2014, [29]) for the numerical computations of the tangent map on SE(3). The vector $\boldsymbol{\mathcal{E}}$ may be regarded as the geometric error between the homogeneous transformations $\boldsymbol{g}_d$ and $\boldsymbol{g}_L$ such that if $\boldsymbol{g}_d = \boldsymbol{g}_L$ will simply yield $\|\boldsymbol{\mathcal{E}}\|_2 = 0$. Furthermore, the controller gains λ_1 and λ_2 can be tuned accordingly to tweak the desired transient behavior of the closed-loop system, similar to a classical PD controller.

4.4   Simulation studies of bio-inspired robots

In this section, we detail the numerical simulations of the port-Hamiltonian model in (4.36) together with the energy-shaping controller in (4.37). For all numerical simulations, we consider a truncation degree of the ROM model is $k = 8$.

Due to the partial differential nature, we have to employ a nested ODE routine to recover the trajectories for $\boldsymbol{q}$ and $\boldsymbol{p}$. First, we employ an implicit trapezoidal solver with a fixed stepsize of $dt = 30$ ms to solve (4.36). At each time increment, we have to evaluate the dynamic matrices (4.22)-(4.26). To efficiently compute these dynamic entities, we solve the spatial integration problem over the material domain $\mathbb{X}$ by using a second-order Runge-Kutta solver. The stepsize for the spatial solver is $d\sigma = 5$ mm. All simulation examples and underlying source code are provided publicly on the `SOROTOKI` toolkit [30]. Here, the numerical integrations of the system matrices (4.22), (4.23), (4.25) and (4.26) are performed using a so-called Matrix-Differential solver (see [1]). The simulations are performed on a modern machine (Ryzen 7-5800H, 3.2GHz).

For the soft robotic simulations, we have chosen a linear isotropic Hookean material with shear constraints. Given these material properties, the inertia tensor and the stiffness tensor become diagonal matrices:

$$\boldsymbol{\mathcal{M}} = \text{blkdiag}\left\{\rho_0 \boldsymbol{\mathcal{J}}, \ \rho_0 A \boldsymbol{I}_3\right\};$$

$$\boldsymbol{\mathcal{K}} = \text{blkdiag}\left\{\mu_1 \boldsymbol{\mathcal{J}}, \ EA, \ \mu_2 A, \ \mu_2 A\right\},$$

where the (average) cross-sectional is $A = \pi r^2$ for a disc radius r, and $\boldsymbol{\mathcal{J}}$ the second moment of area. The damping tensor chosen as $\boldsymbol{\mathcal{D}} = \zeta \boldsymbol{\mathcal{K}}$ with damping coefficient ζ. The visco-elastic matrices are precomputed using (4.27) and (4.28).

4.4.1   Soft robot manipulator inspired by octopus' tentacle

In the first study-case, we consider a soft robotic arm that is loosely inspired by the tentacles of an octopus. To introduce the under-actuation typically present in soft robotics, we have chosen an actuation matrix $\boldsymbol{G} = \text{blkdiag}\left\{\boldsymbol{I}_5, \boldsymbol{O}_3\right\}$ such that only the first five modes are actively controllable. The system properties can shown in Table 4.1. The soft robot is subjected to the energy-based controller in (4.37), where the control gains are tuned to produce a smooth transient: $\lambda_1 = 0.01$ and $\lambda_2 = 0.001$. The artificial spring stiffness is chosen as $\boldsymbol{k}_p = \text{blkdiag}\left\{0.01 \cdot \boldsymbol{I}_3, \boldsymbol{I}_3\right\}$. Lastly, the desired configuration of the end-effector is chosen as follows:

$$\boldsymbol{g}_d = \begin{pmatrix} \boldsymbol{I}_3 & \boldsymbol{r}_d \\ \boldsymbol{0}_3^\top & 1 \end{pmatrix} \quad \text{with} \quad \boldsymbol{r}_d = \begin{pmatrix} 0.04 \\ 0.00 \\ -0.01 \end{pmatrix}.$$

Table 4.1. Parameters setting for the numerical solver, the soft manipulator, and the energy-based controller.

Parameter description	Symbol	Value	Unit
Finite horizon time	T	10	s
Intrinsic length	L	120	mm
Cross-section radius	r	8.25	mm
Uniform density	ρ_0	1250	kgm^{-3}
Young's modulus	E	25	MPa
Shear modulus	μ_1	10	MPa
Constraint modulus	μ_2	15	GPa
Rayleigh coefficient	ζ	0.40	-

The numerical results of the closed-loop system are shown in Figure 4.3 and 4.4. It is worth mentioning that these simulation run at ±120 Hz real-time.[1]

Figure 4.3 shows the evolution of the continuous deformation along the soft robotic body, whereas Figure 4.4 shows the modal coefficients $\boldsymbol{q}(t)$ and generalized momenta $\boldsymbol{p}(t)$. As can be seen, the end-effector of the soft robot manipulator slowly converges to the desired set-point $\boldsymbol{g}_d \in \text{SE}(3)$. Although the control gains could be increased to promote a faster transient, it was observed that high gains lead to undesired (propagating) oscillations of the flexible structure. A possible solution might be to introduce negative damping to the controller Hamiltonian $\mathcal{H}_d$, to overcome the soft robot's structural damping.

For the second simulation run, we modified the control gains to highlight an interesting property of the proposed controller. To be more specific, we increase the controller gains to $\lambda_1 = \lambda_2 = 0.1$. The numerical results for the increased controller gains are shown in Figure 4.5 and Figure 4.6. Although the control goal and the initial conditions are chosen identical, the soft robot converges to a different configuration – albeit, a shape with less '*complexity*'. The cause of less complicated bending patterns has two origins. First, increasing the control gains also artificially impacts the structural stiffness of the soft robot, resulting in soft robot with a higher perceived stiffness. Second, by increasing the stabilizing term λ_2 in the damped Jacobian inverse (4.38), more weight is given towards finding a solution that also minimizes the joint angles $\|\boldsymbol{q}\|_2$. As intrinsically, more energy is spent to excite higher-order modes in the basis $\{\theta_n\}_{n=1}^k$, the energy-based controller will thus find a minimizer that accounts for the ordering of the shape basis, penalizing higher-order modes. This result indicates that the proposed controller can be effectively tuned alter the structural compliance of the soft robot; and thus could be implemented carefully to preserve '*softness*'.

---

[1]Real-time bandwidth is determined by the ratio between finite horizon and CPU's computation time, *i.e.*, $f \approx T/T_{\text{sim}}$, which is affected most by spatial stepsize due to explicit integration.
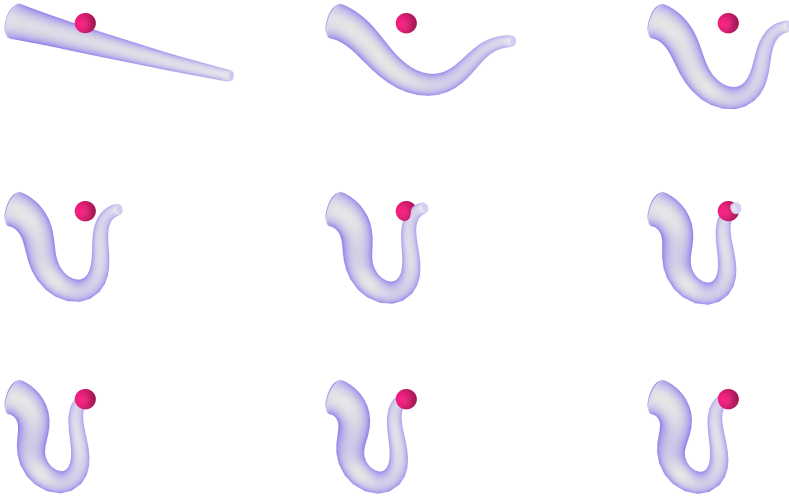
Figure 4.3. Three-dimensional evolution of the soft robot manipulators, slowly converging to the desired set-point $g_d \in \mathrm{SE}(3)$ (indicated by the pink ball). Please observe the morphology that arises which can be related to the motion of an octopus.
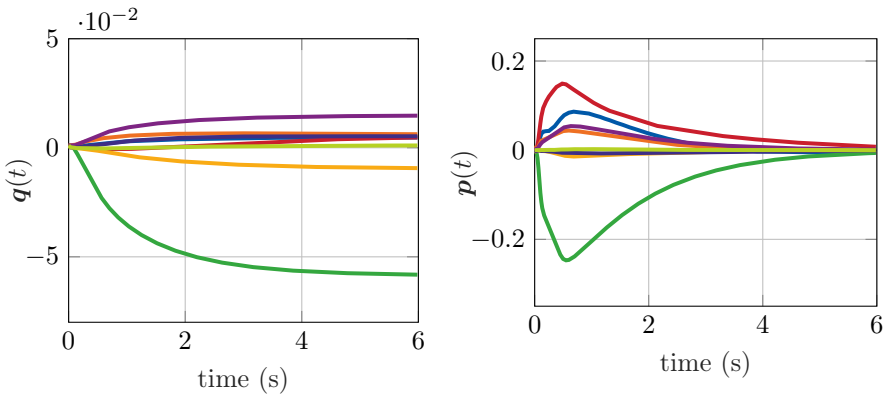

Figure 4.4. The evolution of the modal coefficients and the generalized momenta of the soft robot manipulator. The modal coefficients $\boldsymbol{q}$ are ordered as follows $\{q_1, ..., q_8\} = \{\textcolor{blue}{\blacksquare}, \textcolor{red}{\blacksquare}, \textcolor{green}{\blacksquare}, \textcolor{orange}{\blacksquare}, \textcolor{purple}{\blacksquare}, \textcolor{orange}{\blacksquare}, \textcolor{purple}{\blacksquare}, \textcolor{green}{\blacksquare}\}$. Observe that mainly mode 3 is dominant.
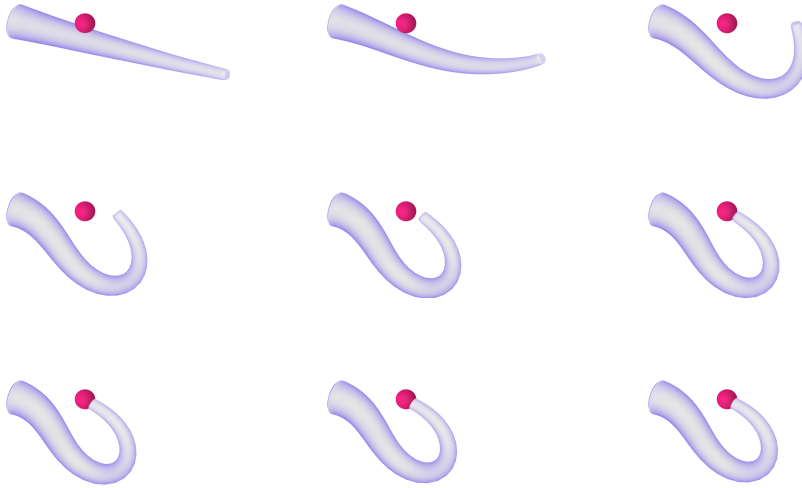
Figure 4.5. Three-dimensional evolution of the soft robot manipulators, slowly converging to the desired set-point $g_d \in \mathrm{SE}(3)$ (indicated by the pink ball). Please observe that a different morphology arises due to higher control gains, *i.e.*, $\lambda_1 = \lambda_2 = 0.1$, which is caused by the controller affecting the structural compliance of the soft robot.
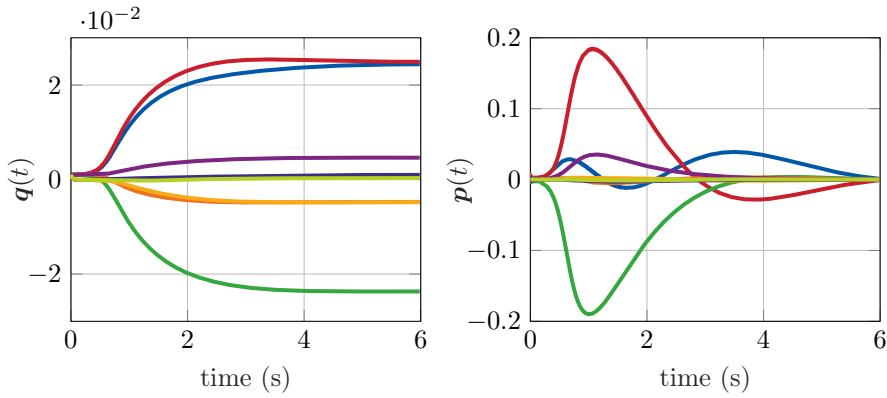

Figure 4.6. The evolution of the modal coefficients and the generalized momenta of the soft robot manipulator with the increased controller gains. The modal coefficients q are ordered as follows $\{q_1, ..., q_8\} = \{ \text{—}, \text{—}, \text{—}, \text{—}, \text{—}, \text{—}, \text{—}, \text{—} \}$. Observe now that the modes 1,2, and 3 are dominant.

4.4.2 Multi-link soft robot inspired by the elephant's trunk

In the second study-case, we consider a two-link soft robot that is inspired by the trunk of an elephant. A similar soft robotic system is considered in [4] (*i.e.*, the elephant-inspired bionic arm by `Festo`), where mobility of the bio-inspired robotic system is achieved through a pneumatic-network distributed along the continuous body of the robot. Therefore, considering a six-bellow network, the actuation matrix takes the form:

$$\boldsymbol{G}(\boldsymbol{q})\boldsymbol{u} = \sum_{n=1}^{6} \left[\int_{\mathbb{X}} [\boldsymbol{J}]_k(\sigma, \boldsymbol{q}) \cdot \boldsymbol{\mathcal{F}}_n(\sigma) \, d\sigma \right] u_i,$$

where $\{\boldsymbol{\mathcal{F}}_n\}_{n=1}^{6}$ is a set of piece-wise constant wrench functionals related to the pneumatic actuation bellows distributed along the soft robotic body, and $\boldsymbol{u} = (u_1, u_2, u_3, u_4, u_5, u_6)^{\top}$ a vector of wrench amplitudes. The control input sets $\{u_1, .., u_3\}$ relate to the first link and $\{u_4, .., u_6\}$ to the second link of the robot. Given this input configuration, it also follows that $\text{rank}(\boldsymbol{G}(\boldsymbol{q})) < \dim(\boldsymbol{q})$ for all $\boldsymbol{q} \in \mathbb{R}^{6k}$, *i.e.*, underactuated. The system and solver properties are given in Table 4.2. We again consider $k = 8$ spatial modes. To simulate the effect of the gripper, we added an inertial mass at the end-effector modelled by:

$$\boldsymbol{\tau}_{\text{ext}} = \boldsymbol{\mathcal{M}}_{\text{grip}} \boldsymbol{J}(\boldsymbol{q}, L)^{\top} \left[\left(\boldsymbol{0}_3^{\top}, \, \boldsymbol{a}_g^{\top} \mathbf{Ad}_{\boldsymbol{g}(\cdot, L)}^{\top} \right)^{\top} + \dot{\boldsymbol{\eta}}(\boldsymbol{q}, L) \right],$$

where $\boldsymbol{\mathcal{M}}_{\text{grip}}$ inertia tensor related to the gripper placed at the end-effector of the robot located at $\sigma = L$. Again we apply the energy-based controller in (4.37) to the system, where the control gains are $\lambda_1 = 5$ and $\lambda_2 = 1$, while the artificial stiffness matrix $\boldsymbol{k}_p$ is kept identical to previous simulations. Lastly, the desired configuration of the end-effector is chosen as follows:

$$\boldsymbol{g}_d = \begin{pmatrix} \boldsymbol{\Phi}_d & \boldsymbol{r}_d \\ \boldsymbol{0}_3^{\top} & 1 \end{pmatrix} \quad \text{with} \quad \boldsymbol{r}_d = \begin{pmatrix} 0.125 \\ 0.100 \\ 0.175 \end{pmatrix} \quad \text{and} \quad \boldsymbol{\Phi}_d = \text{Rot}_y\left(\frac{1}{4}\pi\right).$$

The numerical results of the closed-loop system are shown in Figure 4.7 and Figure 4.8 which could reach a real-time performance of ± 65Hz. Figure 4.7 shows the continuous deformation along the soft robotic body. Figure 4.8 shows the trajectories of the modal coefficients $\boldsymbol{q}(t)$ and the generalized momenta $\boldsymbol{p}(t)$. As can be seen, the end-effector of the soft robot manipulator slowly converges to the desired set-point $\boldsymbol{g}_d \in \text{SE}(3)$, even when dealing with piece-wise distributed actuation loads applied to the continuous backbone. To describe the discontinuous actuation profiles, however, higher order modes are required as can be seen in Figure 4.8. This might indicate there exist better tailored compact shape bases for this soft robotic system.
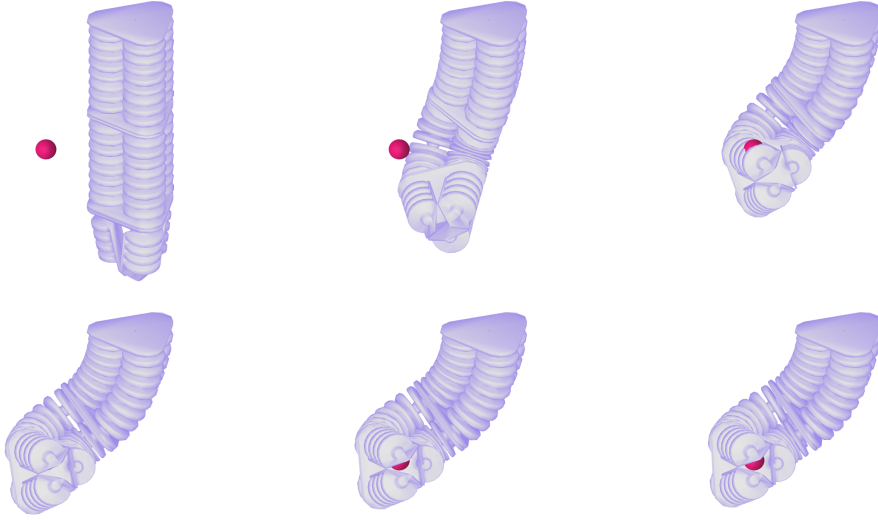
Figure 4.7. Three-dimensional evolution of the soft robot inspired by the elephant's trunk (whose muscular network is mimicked through six pneumatic bellows), slowly converging to the desired set-point $\boldsymbol{g}_d \in \mathrm{SE}(3)$ (*i.e.*, the pink ball).

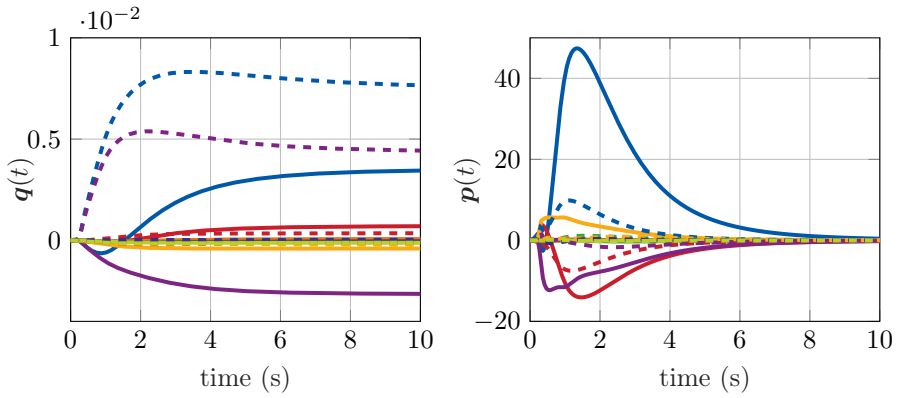**Figure 4.8.** The evolution of the modal coefficients and the generalized momenta of the soft robot manipulator inspired by the elephant's trunk. The modal coefficients $\boldsymbol{q}$ are ordered as follows $k \in \{1, ..., 8\} = \{$ ▬, ▬, ▬, ▬, ▬, ▬, ▬, ▬ $\}$ where the full and dashed lines represent the first and second link, respectively. Observe that mainly modes 1 and 5 are dominant in both links.

Table 4.2. Parameters setting for the numerical solver, the soft manipulator by the elephant's trunk, and the energy-based controller.

Parameter description	Symbol	Value	Unit
Finite horizon time	T	20	s
Intrinsic length	L	360	mm
Cross-section radius	r	25	mm
Uniform density	ρ_0	250	kgm^{-3}
Young's modulus	E	35	MPa
Shear modulus	μ_1	20	MPa
Constraint modulus	μ_2	15	GPa
Rayleigh coefficient	ζ	0.45	-

4.5   Concluding remarks

Due to their intrinsic compliance of soft robots, they allow for complex morphological motions that mimic animals in nature. Achieving similar performance to biology highlights the need for more accurate dynamic models and control strategies. In this chapter, we provided a modeling framework for Cosserat beams that leads to a finite-dimensional system in a port-Hamiltonian structure. By exploiting the passivity, an energy-shaping controller was proposed that ensures the closed-loop Hamiltonian is minimal at the desired set-point. The numerical model was developed for a several bio-inspired soft robot (octopus' tentacle and elephant's trunk) with distributed control inputs. The key challenges here regarding both the model as the controller are their ability to capture the hyper-flexibility, deal with inherent under-actuation, and exploit its hyper-redundancy to achieve its control task. Given appropriate controller gains, the model-based controller yields smooth convergence of the soft robot's end-effector while accounting for under-actuation. It was shown that by tuning the controller gains, the intrinsic stiffness of the soft body can be adapted, resulting in significantly different quasi-static joint solutions of the set-point problem. To some extent, the mobility of the Cosserat model paired with the energy-based control has a (close) resemblance to the biological motion. There are, however, a few limitations to our approach. The strain parametrization of functional basis does not account for the geometry of the soft robot, meaning some systems require many spatial modes to *accurately* represent the true continuum dynamics. Second, regarding implementation, measuring these spatial modes in an experimental setting is difficult, and future research is required to find a suitable '*soft sensing*' technique that *(i)* has limited impact on the dynamics, and *(ii)* accounts for the continuity of the elastic body. A possible solution might be the optimal placement of a network of distributed localized sensors, *e.g.,* strain

gauges or IMUs. Furthermore, the proposed controller is only suited for set-point regulation or slow-varying references. Exploring (fast)-dynamic control objectives will likely require more research. In particular, controllers that suppress natural resonances of continuum elastic body under fast motion. One could argue that this perhaps fights against the natural dynamics of the soft robot, yet such oscillations might be able to be explored for locomotion or soft manipulators throwing objects rather than traditional pick-and-place strategies.

Given these limitations, future work will focus on the following: *(i)* hyper-elasticity *(ii)* validating the controller experimentally, and *(iii)* constructing a set of basis functions through the so-called "*snapshot decomposition method*" using FEM-driven data. In particular, the latter two goals could be interesting to explore. Both advantages in FEM and Cosserat models, being accurate continuum deformations and computational efficiency; leading to a modeling strategy for *optimal* finite-dimensional state projection with insightful structure of the passive and active joints.

4.A   Supplementary material

4.A.1   Basic definitions on Lie group and Lie algebra

Here we briefly discuss some notation and basic operations on the Lie groups SO(3) and SE(3), and their respective Lie algebras so(3) and se(3). This appendix serves a compact comprehensive introduction in the context of robotics, and the appendix is based on the comprehensive work of Bullo and Murray (1995, [26]).

(*Basic definition(s)*). Here, we focus first on the (Lie) group of rigid-body transformations about the origin of $\mathbb{R}^3$ – denoted by SE(3). Let $G \subset$ SE(3) be a matrix Lie group and its respective algebra $\mathfrak{g} \in$ se(3) its Lie Algebra. Then, the evolution of a general rigid body under motion with pose $\boldsymbol{g} \in G$ can be described using

$$\dot{\boldsymbol{g}} = \boldsymbol{g}\,\hat{\boldsymbol{\eta}}^{\mathrm{b}} \iff \dot{\boldsymbol{g}} = \hat{\boldsymbol{\eta}}^{\mathrm{s}}\,\boldsymbol{g}. \quad \hat{\boldsymbol{\eta}}^{\mathrm{b}}, \hat{\boldsymbol{\eta}}^{\mathrm{s}} \in \mathfrak{g} \tag{4.39}$$

where the velocity twist relative its body frame is given by $\hat{\boldsymbol{\eta}}^{\mathrm{b}}$ or to a spatial frame by $\hat{\boldsymbol{\eta}}^{\mathrm{s}}$. Since $\dot{\boldsymbol{g}} = \boldsymbol{g}\hat{\boldsymbol{\eta}}^{\mathrm{b}}$ is invariant under left multiplication by constant matrices, we call it *left invariant*; and correspondingly $\dot{\boldsymbol{g}} = \hat{\boldsymbol{\eta}}^{\mathrm{s}}\boldsymbol{g}$ is said to be *right invariant*. Let it be clear that the geometric strain $\boldsymbol{\xi}(\sigma, t)$ and velocity twist $\boldsymbol{\eta}(\sigma, t)$ in (4.2) and (4.3) are thus expressed in the body frame. Next, let us discuss the adjoint actions. For all $\boldsymbol{g} \in G$ and any $\boldsymbol{X}, \boldsymbol{Y} \in \mathfrak{g}$, the adjoint action $\mathbf{Ad}_{\boldsymbol{g}}$ and the matrix commutator or adjoint action on the algebra $\mathbf{ad}_{\boldsymbol{X}}$ are defined as

$$\mathbf{Ad}_{\boldsymbol{g}}\boldsymbol{X} = \boldsymbol{g}\boldsymbol{X}\boldsymbol{g}^{-1} \tag{4.40}$$

$$\mathbf{ad}_{\boldsymbol{X}}\boldsymbol{Y} = [\boldsymbol{X}, \boldsymbol{Y}] = \boldsymbol{X}\boldsymbol{Y} - \boldsymbol{Y}\boldsymbol{X}. \tag{4.41}$$

Now, on SE(3) and se(3) we represent a matrix group element $\boldsymbol{g} = (\boldsymbol{\Phi}, \boldsymbol{\gamma}) \in$ SO(3) $\times \mathbb{R}^3 \cong$ SE(3) and a (velocity) twist vector field $\hat{\boldsymbol{\eta}} = (\boldsymbol{\Omega}, \boldsymbol{V}) \in$ se(3) using homogenous coordinates,

$$\boldsymbol{g} := \begin{pmatrix} \boldsymbol{\Phi} & \boldsymbol{\gamma} \\ \boldsymbol{0}_3^\top & 1 \end{pmatrix}; \quad \hat{\boldsymbol{\eta}} := \begin{pmatrix} \boldsymbol{\Omega}^\times & \boldsymbol{V} \\ \boldsymbol{0}_3^\top & 1 \end{pmatrix}. \tag{4.42}$$

where the operator $(\cdot)^\times : \mathbb{R}^3 \to$ so(3) is defined such that $\boldsymbol{x}^\times \boldsymbol{y} = \boldsymbol{x} \times \boldsymbol{y}$ for all $\boldsymbol{x}, \boldsymbol{y} \in \mathbb{R}^3$, and $(\cdot)^\wedge : \mathbb{R}^6 \to$ se(3). Now, representing the geometric twist as a column vector $\boldsymbol{\eta}^\wedge \to \boldsymbol{\eta}$, it straightforwardly follows from (4.40) and (4.41) that the adjoint actions can be written in the form:

$$\mathbf{Ad}_{\boldsymbol{g}} := \begin{pmatrix} \boldsymbol{\Phi} & \boldsymbol{0}_{3\times 3} \\ \boldsymbol{\gamma}^\times \boldsymbol{\Phi} & \boldsymbol{\Phi} \end{pmatrix}; \quad \mathbf{ad}_{\boldsymbol{\eta}} := \begin{pmatrix} \boldsymbol{V}^\times & \boldsymbol{0}_{3\times 3} \\ \boldsymbol{\Omega}^\times & \boldsymbol{V}^\times \end{pmatrix}. \tag{4.43}$$

The notation above are analogous to the notations used in Chapter 3.

(*Exponential and logarithmic map*). An important operation in Lie group theory, is the exponential and logarithmic maps that serve as transformations between the groups and their respective algebras. Lets start with the exponential map. Given $\boldsymbol{\Omega}^\times \in$ so(3) and $\boldsymbol{\eta} = (\boldsymbol{\Omega}, \boldsymbol{V}) \in$ se(3), the exponential maps for the orientation group $\exp_{\text{SO}(3)} :$ so(3) $\to$ SO(3) and the rigid-body transformation group $\exp_{\text{SO}(3)} :$ se(3) $\to$ SE(3) are given respectively by

$$\exp_{\text{SO}(3)}(\boldsymbol{\Omega}) = \boldsymbol{I} + \sin\|\boldsymbol{\Omega}\| \frac{\boldsymbol{\Omega}^\times}{\|\boldsymbol{\Omega}\|} + (1 - \cos\|\boldsymbol{\Omega}\|) \frac{\boldsymbol{\Omega}^\times \boldsymbol{\Omega}^\times}{\|\boldsymbol{\Omega}\|^2}; \tag{4.44}$$

$$\exp_{\text{SE}(3)}(\boldsymbol{\xi}) = \begin{pmatrix} \exp_{\text{SO}(3)}(\boldsymbol{\Omega}) & A(\boldsymbol{\Omega})\boldsymbol{V} \\ \boldsymbol{0}_3^\top & 1 \end{pmatrix}, \tag{4.45}$$

where $\|\cdot\|$ stands for the Euclidean norm and the operator $A(\boldsymbol{\Omega})$ is given By

$$A(\boldsymbol{\Omega}) = \boldsymbol{I} + \left(\frac{1 - \|\boldsymbol{K}\|}{\|\boldsymbol{K}\|} \right) \frac{\boldsymbol{\Omega}^\times}{\|\boldsymbol{\Omega}\|} + (1 - \sin\|\boldsymbol{\Omega}\|) \frac{\boldsymbol{\Omega}^\times \boldsymbol{\Omega}^\times}{\|\boldsymbol{\Omega}\|^2}. \tag{4.46}$$

Note that we have seen equation (4.44) earlier which is known as the Rogdrigues' formula. Referring to [26], in an open neighborhood of the origin in G, we define $\boldsymbol{\eta} = \log(\boldsymbol{g}) \in \mathfrak{g}$ to be the '*exponential coordinates*' of the group element $\boldsymbol{g}$. Then, the logarithmic map can be regarded as the local chart of the manifold G. As such, let $\boldsymbol{g} = (\boldsymbol{\Phi}, \boldsymbol{\gamma}) \in$ SO(3) $\times \mathbb{R}^3$ be such that trace($\boldsymbol{\Phi}$) $\neq -1$. Then, the logarithmic map $\log_{SO3} :$ SO(3) $\to$ so(3) is given by

$$\log_{\text{SO}(3)}(\boldsymbol{\Phi}) = \frac{\theta}{2\sin\theta}(\boldsymbol{\Phi} - \boldsymbol{\Phi}^\top), \tag{4.47}$$

where the angle θ satisfies $\cos\theta = \frac{1}{2}(\text{trace}(\boldsymbol{\Phi}) - 1)$ and is bounded by $|\theta| < \pi$. Following (4.47), and logarithmic map $\log_{SE3} : \text{SE}(3) \to \text{se}(3)$ is then given by

$$\log_{\text{SE}(3)}(\boldsymbol{g}) = \begin{pmatrix} \boldsymbol{\Omega}^{\times} & A^{-1}(\boldsymbol{\Omega})\boldsymbol{\gamma} \\ \boldsymbol{0}_3^{\top} & 1 \end{pmatrix}, \tag{4.48}$$

where $\boldsymbol{\Omega}^{\times} = \log_{\text{SO}(3)}(\boldsymbol{\Phi})$ and the mapping $A^{-1}(\boldsymbol{\Omega})$ is given By

$$A^{-1}(\boldsymbol{\Omega}) = \boldsymbol{I} - \frac{1}{2}\boldsymbol{\Omega}^{\times} + \left[1 - \frac{\|\boldsymbol{\Omega}\|}{2} \cot\left(\frac{\|\boldsymbol{\Omega}\|}{2}\right) \right] \frac{\boldsymbol{\Omega}^{\times}\boldsymbol{\Omega}^{\times}}{\|\boldsymbol{\Omega}\|^2}, \tag{4.49}$$

where $\cot : \mathbb{R} \to \mathbb{R}$ is the co-tangent function.

4.A.2   Time-derivation of geometric manipulator Jacobian

The mapping from generalized coordinates $\dot{\boldsymbol{q}} \in \mathbb{R}^n$ to the velocity-twist vector $\hat{\boldsymbol{\eta}} = \boldsymbol{g}^{-1}\dot{\boldsymbol{g}} \in \text{se}(3) \cong \mathbb{R}^6$ for a point σ be given by $\boldsymbol{\eta} = \boldsymbol{J}\dot{\boldsymbol{q}}$ where $\boldsymbol{J}$ is the geometric Jacobian. The k-th order truncations of the exact geometric Jacobian is given by

$$[\boldsymbol{J}]_k = \mathbf{Ad}_{[g]_k}^{-1} \int_0^{\sigma} \mathbf{Ad}_{[g]_k} \boldsymbol{\Theta} \, ds. \tag{4.50}$$

Unlike its notation in rigid robotics, note that the geometric Jacobian matrix here is time and space-variant. Following the chain rule of differentiation, the partial time-derivative of the geometric Jacobian matrix yields

$$[\dot{\boldsymbol{J}}]_k = \left(\dot{\mathbf{Ad}}_{[\boldsymbol{g}]_k}^{-1} \right) \int_0^{\sigma} \mathbf{Ad}_{[g]_k} \boldsymbol{\Theta} \, ds + \mathbf{Ad}_{[g]_k}^{-1} \int_0^{\sigma} \left(\dot{\mathbf{Ad}}_{[g]_k} \right) \boldsymbol{\Theta} \, ds. \tag{4.51}$$

Given the differential relations of the adjoint action mapping on the Lie group, that is, $d/ds\,(\mathbf{Ad}_{\boldsymbol{g}}) = \mathbf{Ad}_{\boldsymbol{g}}\mathbf{ad}_{\boldsymbol{\Upsilon}}$ given a twist $\boldsymbol{\Upsilon} = (\boldsymbol{g}^{-1}d\boldsymbol{g}/ds)^{\vee}$, we can express the time-derivate of the adjoint action and its inverse as

$$\frac{\partial}{\partial t}(\mathbf{Ad}_{\boldsymbol{g}}) = \mathbf{Ad}_{\boldsymbol{g}}\mathbf{ad}_{\boldsymbol{\eta}}, \tag{4.52}$$

$$\frac{\partial}{\partial t}(\mathbf{Ad}_{\boldsymbol{g}^{-1}}) = -\mathbf{ad}_{\boldsymbol{\eta}}\mathbf{Ad}_{\boldsymbol{g}^{-1}}. \tag{4.53}$$

Substituting the truncated variations of (4.52) and (4.53) into (4.51), we find the complete expression of the time-derivate of the geometric Jacobian matrix

$$[\dot{\boldsymbol{J}}]_k = -\mathbf{ad}_{\boldsymbol{\eta}}[\boldsymbol{J}]_k + \mathbf{Ad}_{[g]_k}^{-1} \int_0^{\sigma} \mathbf{Ad}_{[g]_k}\mathbf{ad}_{[\boldsymbol{\eta}]_k} \boldsymbol{\Theta} \, ds. \tag{4.54}$$

Since $\mathbf{ad}_{\boldsymbol{\eta}}(\boldsymbol{J}\dot{\boldsymbol{q}}) = \mathbf{ad}_{\boldsymbol{\eta}}\boldsymbol{\eta} = \boldsymbol{0}_6$ by definition, the first right-hand term vanishes if (4.54) is post-multiplied with the generalized velocities $\dot{\boldsymbol{q}}$, thus leading to the acceleration twist $[\dot{\boldsymbol{\eta}}]_k$ in (4.16).

Bibliography

[1] B. Caasenbrood, A. Pogromsky, and H. Nijmeijer, "Control-Oriented Models for Hyperelastic Soft Robots Through Differential Geometry of Curves," *Soft Robotics*, vol. 0, no. 0, 2022.

[2] B. Caasenbrood, A. Y. Pogromsky, and H. Nijmeijer, "Energy-based control for soft manipulators using cosserat-beam models," in *International Conference on Informatics in Control, Automation and Robotics - ICINCO*, pp. 311–319, 2021.

[3] W. Choi, G. M. Whitesides, M. Wang, X. Chen, R. F. Shepherd, A. D. Mazzeo, S. A. Morin, A. A. Stokes, and F. Ilievski, "Multigait soft robot," *Proceedings of the National Academy of Sciences*, vol. 108, no. 51, pp. 20400–20403, 2011.

[4] V. Falkenhahn, T. Mahl, A. Hildebrandt, R. Neumann, and O. Sawodny, "Dynamic Modeling of Bellows-Actuated Continuum Robots Using the Euler-Lagrange Formalism," *IEEE Transactions on Robotics*, vol. 31, no. 6, pp. 1483–1496, 2015.

[5] A. D. Marchese, C. D. Onal, and D. Rus, "Autonomous Soft Robotic Fish Capable of Escape Maneuvers Using Fluidic Elastomer Actuators," *Soft Robotics*, vol. 1, no. 1, pp. 75–87, 2014.

[6] C. Duriez, "Control of elastic soft robots based on real-time finite element method," pp. 3982–3987, Proceedings - IEEE International Conference on Robotics and Automation, 2013.

[7] F. Largilliere, V. Verona, E. Coevoet, M. Sanz-Lopez, J. Dequidt, and C. Duriez, "Real-time control of soft-robots using asynchronous finite element modeling," *Proceedings - IEEE International Conference on Robotics and Automation*, vol. 2015-June, no. June, pp. 2550–2555, 2015.

[8] K. Wu and G. Zheng, "FEM-Based Gain-Scheduling Control of a Soft," *Robotics and Automation Letters*, vol. 6, no. 2, pp. 3081–3088, 2021.

[9] M. W. Spong, S. Hutchinson, and M. Vidyasagar, *Robot modeling and control*. New York: John Wiley & Sons, 2006.

[10] R. M. Murray, Z. Li, and S. S. Sastry, *A Mathematical Introduction to Robotic Manipulation*, vol. 29. 1994.

[11] J. Till, V. Aloi, and C. Rucker, "Real-time dynamics of soft and continuum robots based on Cosserat rod models," *International Journal of Robotics Research*, vol. 38, no. 6, pp. 723–746, 2019.

[12] C. Della Santina, C. Duriez, and D. Rus, "Model Based Control of Soft Robots: A Survey of the State of the Art and Open Challenges," pp. 1–69, 2021.

[13] Z. Zhang, T. M. Bieze, J. Dequidt, A. Kruszewski, and C. Duriez, "Visual servoing control of soft robots based on finite element model," in *2017 IEEE/RSJ International Conference on Intelligent Robots and Systems (IROS)*, pp. 2895–2901, 2017.

[14] R. K. Katzschmann, C. D. Santina, Y. Toshimitsu, A. Bicchi, and D. Rus, "Dynamic motion control of multi-segment soft robots using piecewise constant curvature matched with an augmented rigid body model," *RoboSoft 2019 - 2019 IEEE International Conference on Soft Robotics*, no. February, pp. 454–461, 2019.

[15] C. Della Santina and D. Rus, "Control oriented modeling of soft robots: The polynomial curvature case," *IEEE Robotics and Automation Letters*, vol. 5, no. 2, pp. 290–298, 2020.

[16] F. Renda, C. Armanini, V. Lebastard, F. Candelier, and F. Boyer, "A Geometric Variable-Strain Approach for Static Modeling of Soft Manipulators with Tendon and Fluidic Actuation," *IEEE Robotics and Automation Letters*, vol. 5, no. 3, pp. 4006–4013, 2020.

[17] F. Boyer, V. Lebastard, F. Candelier, and F. Renda, "Dynamics of Continuum and Soft Robots: A Strain Parameterization Based Approach," *IEEE Transactions on Robotics*, vol. 37, no. 3, pp. 847–863, 2021.

[18] D. Bruder, X. Fu, R. B. Gillespie, C. D. Remy, and R. Vasudevan, "Data-driven control of soft robots using koopman operator theory," *IEEE Transactions on Robotics*, vol. 37, no. 3, pp. 948–961, 2021.

[19] J. C. Simo and L. Vu-Quoc, "A three-dimensional finite-strain rod model. part II: Computational aspects," *Computer Methods in Applied Mechanics and Engineering*, vol. 58, no. 1, pp. 79–116, 1986.

[20] F. Renda, F. Boyer, J. Dias, and L. Seneviratne, "Discrete Cosserat Approach for Multisection Soft Manipulator Dynamics," *IEEE Transactions on Robotics*, vol. 34, no. 6, pp. 1518–1533, 2018.

[21] E. Franco and A. Garriga-Casanovas, "Energy-shaping control of soft continuum manipulators with in-plane disturbances," *International Journal of Robotics Research*, 2020.

[22] A. J. Schaft, "Port-Hamiltonian Systems: Network Modeling and Control of Nonlinear Physical Systems," *Advanced Dynamics and Control of Structures and Machines*, vol. 444, no. 1, pp. 127–167, 2004.

[23] R. Ortega, M. W. Spong, F. Gómez-Estern, and G. Blankenstein, "Stabilization of a Class of Underactuated MechanicalSystems Via Interconnection and Damping Assignment," *IEEE Transactions on Automatic Control*, vol. 47, no. 8, pp. 1218–1233, 2002.

[24] R. Ortega, J. A. L. Perez, P. J. Nicklasson, and H. Sira-Ramirez, *Passivity-based Control of Euler-Lagrange Systems: Mechanical, Electrical and Electromechanical Applications.* London, England, UK: Springer, Sept. 1998.

[25] B. Caasenbrood, "SOROTOKI - an open-source soft robotics toolkit for matlab," GitHub, 2020.

[26] F. Bullo and R. M. Murray, "Proportional Derivative (PD) Control on the Euclidean Group," *California Institute of Technology*, Jan. 1995.

[27] F. Boyer, M. Porez, and A. Leroyer, "Poincaré–Cosserat Equations for the Lighthill Three-dimensional Large Amplitude Elongated Body Theory: Application to Robotics," *Journal of Nonlinear Science*, vol. 20, pp. 47–79, Feb. 2010.

[28] P. Astrid, S. Weiland, K. Willcox, and T. Backx, "Missing point estimation in models described by proper orthogonal decomposition," *IEEE Transactions on Automatic Control*, vol. 53, no. 10, pp. 2237–2251, 2008.

[29] V. Sonneville, A. Cardona, and O. Brüls, "Geometrically exact beam finite element formulated on the special Euclidean group SE(3)," *Computer Methods in Applied Mechanics and Engineering*, vol. 268, pp. 451–474, 2014.

[30] B. Caasenbrood, A. Pogromsky, and H. Nijmeijer, "Dynamic modeling of hyper-elastic soft robots using spatial curves," *IFAC Proceedings Volumes (IFAC-PapersOnline)*, 2020.